

Vacuum arc thruster operation in magnetic nozzle

Satyajit Chowdhury^a and Igal Kronhaus^b

Aerospace Plasma Laboratory, Faculty of Aerospace Engineering, Technion - Israel Institute of Technology, Haifa, 3200003, Israel

E-mail: ^asatyajit@campus.technion.ac.il ^bkronhaus@technion.ac.il

December 2019

Abstract. Vacuum arc thruster performance in a magnetic nozzle configuration is experimentally characterized. Measurements are performed on a miniature coaxial thruster with an anode inner diameter of 1.8 mm. The magnetic field is produced by a single air coil, 18 mm in diameter. Direct measurement of thrust, mass consumption and arc current are performed. To obtain statistically viable results ≈ 1500 arc pulses are recorded at each measurement point. Cathode mass erosion is measured using laser profilometry for a stationary cathode case. To sustain thruster operation over several measurement cycles, an active cathode feeding system is used. Performance increase over the non-magnetic case is observed. For $0 < B < 0.07$ T the performance increase is attributed mostly to beam collimation. For $B > 0.07$ T further performance increase is attributed to ion acceleration in a magnetic nozzle. For the selected thruster geometry the best thrust to arc power ratio $T/P \approx 9 \mu\text{N/W}$ obtained at $B \approx 0.2$ T. For $B > 0.2$ T the magnetic field suppresses the arc current hence reducing T/P , although thruster efficiency increases to $\approx 4.5\%$.

Keywords: vacuum arc thruster, magnetic field, magnetic nozzle, electric propulsion, micropropulsion

(Some figures may appear in colour only in the online journal)

Submitted to: *Plasma Sources Sci. Technol.*

1. Introduction

Vacuum arc thrusters (VAT) are promising propulsion devices for nano-satellites and CubeSats [1, 2], with a few examples experimentally operated in space. VAT are pulsed-dc devices that utilize an arc discharge, across an insulator, between two electrodes to produce thrust. The main advantages of the VAT compared to other electric propulsion devices is its simplicity and scalability to very low power ~ 1 W without loss to performance. In a VAT the cathode electrode is consumed as propellant during the discharge. The cathode is eroded in localized regions, where the discharge is attached, known as cathodic spots [3]. The metal plasma emitted from these micrometer sized spots is self-consistently accelerated via gas-dynamic expansion [4]. There are two established VAT configuration: coaxial and ring shaped [5], termed according to the shape and placement of the cathode with respect to the anode. It is

well known that addition of external magnetic field can improve VAT performance [6] and the micro-cathode VAT [7], a ring shaped device, is a well studied case. However, less is known about the effect of external magnetic field on coaxial VATs. One problem is the difficulty in operating such devices over larger number of pulses. Recently a coaxial VAT with an active feeding mechanism was introduced, known as the inline-screw-feeding VAT (ISF-VAT) [8, 9]. Using the ISF-VAT allows us for the first time to accurately and reliably evaluate the performance enhancement of coaxial VAT in an external magnetic field.

2. Experimental Setup

2.1. Thruster

The ISF-VAT concept [10] is shown in Fig. 1. It is a coaxial vacuum arc thruster with an active feeding mechanism. A central cathode rod is freely disposed within a concentric insulator tube. A second electrode, positioned at the outer edge of the insulator, functions both as the anode of the dc circuit and as the exit plane of the thruster. To keep the VAT geometry constant during long duration operations, the cathode, connected to a metallic headless screw, is advanced at a precise rate inside the insulator in a helical path. The screw provides also an electrical contact with the thruster body that is under negative potential. With the correct selection of the linear advance rate and screw pitch, a balance between cathode erosion and feeding can be achieved. The helical motion both compensates for the radial as well as the azimuthal cathode erosion patterns. This allows for maintaining near constant thruster geometry throughout the operational life of the thruster as well as improved uniformity of the re-coating process, i.e. the process of replenishing the conducting layer on the cathode-insulator-anode interface.

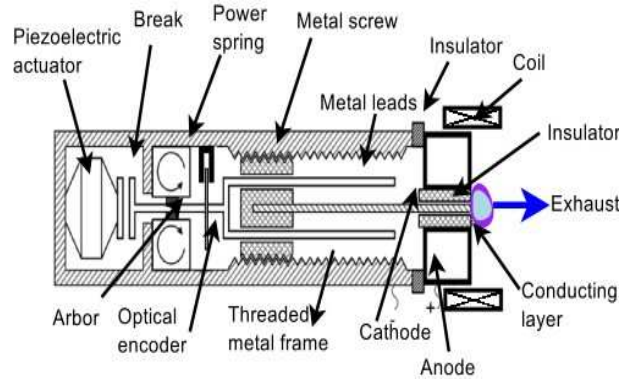


Figure 1: Schematics of the ISF-VAT with added magnetic air coil.

In the present work an ISF-VAT propulsion module (PM) was used. The PM integrates an ISF-VAT with a power processing unit (PPU) and an active feeding system, performing the same set of operations described in Ref. [8] but in miniaturized form. The PM is being developed at the Aerospace Plasma Laboratory (APL), Technion, and is intended for CubeSat use with a total volume of $2.5 \text{ cm} \times 9.6 \text{ cm} \times 9.6 \text{ cm}$ and a “wet” mass of 200 g. The PM is powered by 16 V dc supply.

Following earlier attempts at magnetic enhancement of VATs [6, 11, 12], an air coil wound around the anode was used as the magnetic field source. The coil is formed from a 45 turns of 24 AWG copper wire wound around a teflon bobbin, with an inner diameter of 18 mm and length of 10 mm. The coil is fitted around the ISF-VAT anode and can be relocated along the axis. Typically, to achieve maximum magnetic induction, the coil mid length is aligned flush with the cathode surface.

2.2. Experimental Setup with Propulsion Module and Thrust Balance

The experiments were performed in APL's vacuum chamber, a cylindrical chamber 1.2 m long and 0.6 m in diameter. Two 700 l/s turbo-molecular pumps, each backed by 300 l/m rotary vane pump, are used to maintain a pressure $\sim 10^{-6}$ mbar throughout the test. The chamber pressure is measured by a Pirani gauge. A schematic of the experimental setup is shown in Fig. 2 and a photograph of the setup is shown in Fig. 3. The PM is monitored via serial communication to a PC. The air coil was powered by a dedicated magnetic circuit, placed outside the chamber. The coil current is synchronized by the PM onboard clock and operated only during thruster firing.

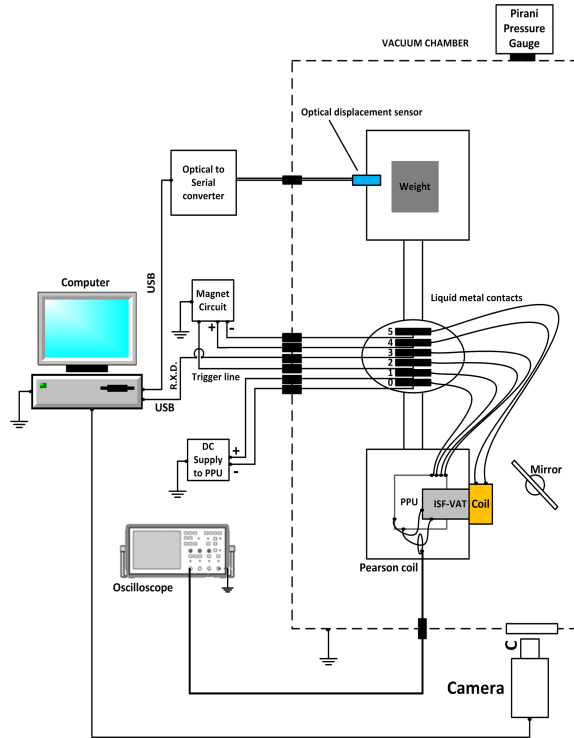


Figure 2: Schematic of the experimental setup.

The PM is placed on a commercial micro-Newton resolution torsion thrust balance [13]. The balance was operated in deflection mode. The deflection signal is transmitted optically and recorded on a PC at a sample rate of 2 Hz. To remove torque bias, the thrust balance was calibrated with the liquid metal bath wiring in

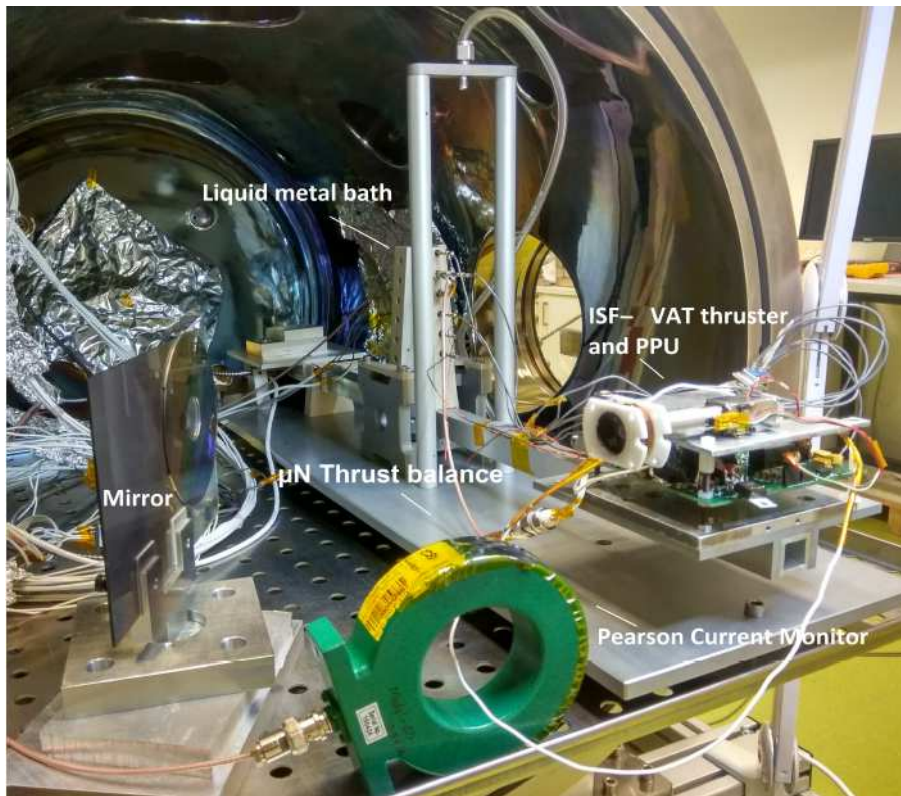


Figure 3: Photograph of the experimental setup, showing the ISF-VAT propulsion module installed on the thrust balance.

the vacuum. An electrostatic force actuator producing known force was used for calibration. Thrust bias was seen to be negligible at all air coil currents.

High temporal resolution measurements of the arc current and arc voltage were manually performed using a Pearson current monitor and a differential high voltage probe (used only when thrust was not measured) recorded on a 5 GS/s oscilloscope. The current of the magnetic air coil was also measured using hall current monitor. Video recording of the plume was performed in each experiment using a charged coupled device (CCD) camera.

3. Experimental Results

3.1. Static Firing Cycles

The first series of experiments were conducted without active feeding, referred here as static firing cycles. The cathode was manually set to flush position (with respect to the anode) and the thruster was operated at arc pulse frequency of $f_p = 17$ Hz for a duration of $t_{fc} = 90$ s. At the end of each firing cycle the thruster was removed from the chamber. To prepare for the next firing cycle the cathode was manually repositioned. Cathode placement was verified using laser profilometry within accuracy

$\sim 10 \mu\text{m}$. This process guarantees consistent initial conditions before each run. The discharge pulse is generated in the following sequence: 1) charging the PPU coil at 35 V for 40 A; 2) then an insulated-gate bipolar transistor (IGBT) switch is opened, the coil voltage reaches $\sim 1 \text{ kV}$; 3) the discharge ignition transitions to an arc in less than $1 \mu\text{s}$.

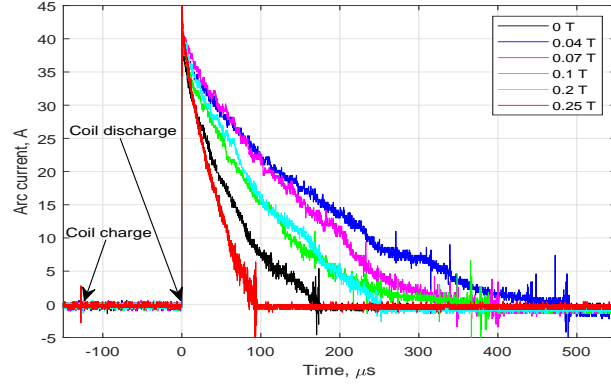


Figure 4: Arc current versus time at different magnetic induction values, each measured during a single pulse. Arrows indicate coil charge and discharge time.

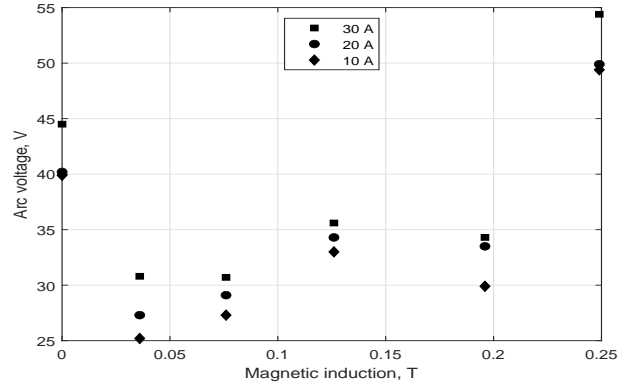


Figure 5: Measured arc voltage versus magnetic induction. Shown are averaged results in the range: 10-20 A (diamond), 20-30 A (circle), 30-40 A (rectangle).

The arc current (I_{arc}) and arc voltage (V_{arc}) were measured simultaneously with a sampling rate of 2.5 MS/s. Fig. 4 shows a typical arc current measurement for different magnetic induction (B) values. In all cases the coil energy and cathode initial conditions are the same. At $B = 0 \text{ T}$ and $B \approx 0.25 \text{ T}$ the arc duration is shorter than for intermediate magnetic induction, these variations are due to change in arc resistance. This is also represented in the average arc voltage as shown in Fig. 5. Here, for convenience, we divided the arc temporal evolution into 3 segments of arc current 10-20 A, 20-30 A, 30-40 A respectively. These segments are used to define the average arc voltage. From these results we can conclude that arc resistance is elevated at $B = 0 \text{ T}$ and $B \approx 0.25 \text{ T}$ compared to intermediate magnetic induction.

The thruster plume, shown in Fig. 6, exhibits significant change in geometry at different magnetic induction values. The plume is hemisphere like at $B = 0$ T whereas at $B \approx 0.12$ T the plume is larger and has a diamond like shape, wider at the base and is pointed in downstream. At the highest magnetic induction tested $B \approx 0.25$ T the plume becomes beam like.

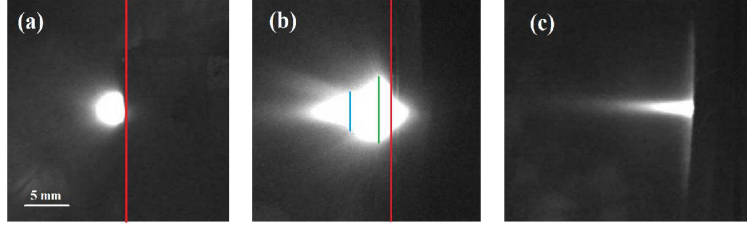


Figure 6: Photographs of the thruster plume (white region) at different magnetic induction values, red line indicate the anode plane. In (a) $B = 0$ and (b) $B \approx 0.12$ T the air coil is upstream to the anode whereas in (c) $B \approx 0.25$ T the coil is at optimum location, downstream of the anode partially blocking the view of the plume. Blue and green lines in (b) represent plume diameter.

In each firing cycle the arc current was recorded with a sampling rate of 50 kS/s. This provided us with 10 - 40 samples per pulse, for a total of $N_p = f_p t_{fc} \approx 1500$ pulses. The total charge Q_{arc} processed by the arc during each run is calculated using a numerical trapezoid integration as follow:

$$Q_{arc} = \int_0^{t_{fc}} I_{arc} dt \quad (1)$$

The cathode mass consumption is measured after each firing cycle using laser profilometry by comparing cathode surface topology before and after firing. This technique is described in detail in Ref. [14]. Fig. 7 shows the cathode mass consumption measurement in two different cross section orientations of the anode-cathode plane (0 degree and 90 degree). The difference in mass measurement for each magnetic induction value is attributed to the non-uniform erosion profile of the cathode.

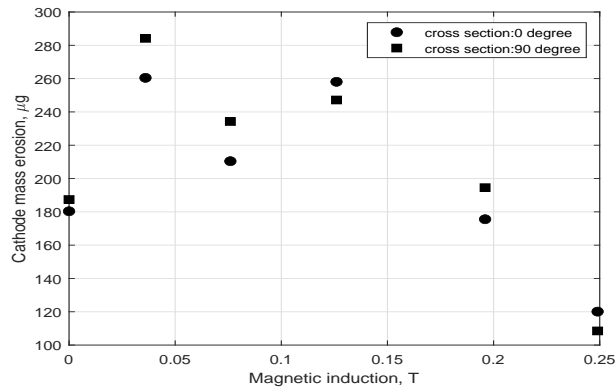


Figure 7: Measured cathode mass erosion versus magnetic induction.

The availability of data on both arc current and mass consumption allows us to

evaluate the erosion rate coefficient E_r as per the given equation:

$$E_r = \frac{\Delta m}{Q_{arc}} \approx \frac{\langle \dot{m} \rangle}{\langle I_{arc} \rangle} \quad (2)$$

where Δm is the total mass consumed in each firing cycle, $\langle \dot{m} \rangle$ is the average mass consumption rate of the cathode, and $\langle I_{arc} \rangle$ is the average arc current. The calculated erosion rate at different magnetic induction values are shown in Fig. 8. We can fit a step like function where $E_r \approx 34 \mu\text{g}/\text{C}$ in the range $B \approx 0.03 - 0.2 \text{ T}$. E_r is reduced for the non-magnetic case and for $B \approx 0.25 \text{ T}$.

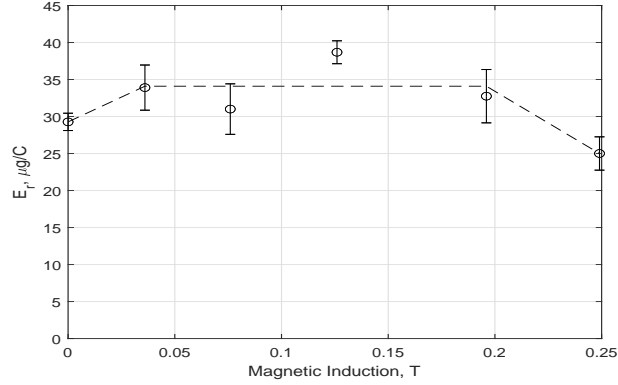


Figure 8: Cathode mass loss per coulomb versus magnetic induction.

Typical time dependant thrust measurements, taken at different magnetic induction values, are shown in Fig. 9. We observe that in all cases thrust is gradually decreasing. This behavior is associated with cathode erosion and is the reason why cathode feeding is necessary for long duration operation.

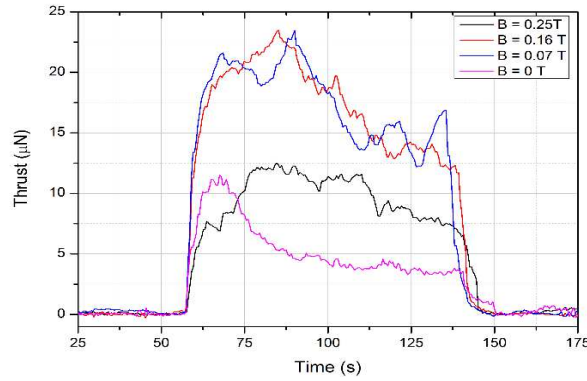


Figure 9: Thrust versus time at several magnetic induction values. Each measured during a single firing cycle. Sample integration time is 0.5 s.

Using the obtained measurements we can evaluate the ion velocity. Assuming a constant ratio between ion current and arc current:

$$f_i = \frac{I_{ion}}{I_{arc}} = \frac{I_{ion} E_r}{\dot{m}} \quad (3)$$

the ion mass flow rate \dot{m}_{ion} can be expressed as:

$$\dot{m}_{ion} = \frac{f_i I_{arc} M_i}{e \langle Z \rangle} \quad (4)$$

where e is the unit charge, $\langle Z \rangle$ is the average charge state of ions and M_i is the ion mass. The thrust is defined as:

$$T = \dot{m}_{ion} \langle u_{i,z} \rangle = \frac{f_i M_i}{e \langle Z \rangle} C_t \langle u_i \rangle I_{arc} \quad (5)$$

where, C_t is beam divergence factor, $\langle u_i \rangle$ is the mean ion velocity and $\langle u_{i,z} \rangle$ is the mean ion velocity perpendicular to the cathode surface. Eq. 5 indicates that the thrust and arc current are correlated. This is indeed observed in Fig. 10 where the normalized time dependent thrust and arc current measurements are overlaid. From Fig. 10 the cross correlation value between T and I_{arc} is:

$$\rho_{TI_{arc}} = \frac{\sigma_{TI_{arc}}}{\sigma_T \sigma_{I_{arc}}} \approx 81 \% \quad (6)$$

where, $\sigma_{TI_{arc}}$ is the covariance, σ_T and $\sigma_{I_{arc}}$ are the thrust and arc current variance.

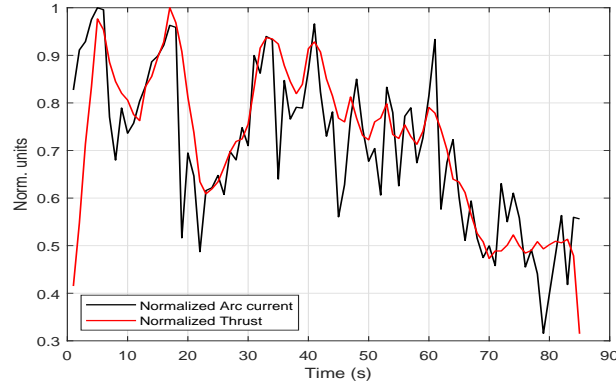


Figure 10: Normalized thrust and arc current versus time, measured during a single firing cycle.

3.2. Dynamic Firing Cycles

In dynamic firing cycles tests the active feeding system is used. The cathode is advanced for a preset encoder steps according to the expected eroded mass. During each firing cycle the arc current was recorded with a sampling rate of 50 kS/s. This provided us with 10-40 samples per pulse and the total charge processed by the arc was calculated from Eq. (1). The average arc power P_{arc} was calculated according to:

$$\langle P_{arc}(B) \rangle = \frac{1}{t_{fc}} Q_{arc} \langle V_{arc}(B) \rangle \quad (7)$$

where the mean arc voltage $\langle V_{arc} \rangle$ as a function of B is presented in Fig. 5. The results are shown in Fig. 11. We observe a nearly constant average P_{arc} , a results that is expected as it represents the inductive energy stored in the PPU coil $\epsilon_L = P_{arc}/f_p \approx 2.2/17 = 130$ mJ that does not depend on the arc quality.

Thrust measurement were performed for dynamic firing cycles. At each magnetic induction, a sequence of 4 firing cycles were performed ≈ 6000 pulses. The time

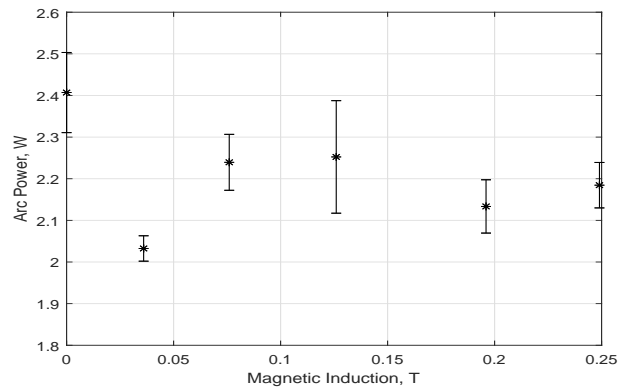


Figure 11: Average arc power versus magnetic induction.

averaged results are shown in Fig. 12. We observe that the thrust increases rapidly for $0 < B < 0.07$ T, reaches a maximum value at $B \approx 0.2$ T, and significantly reduces for $B \approx 0.25$ T. Thrust to arc power ratio T/P_{arc} versus B is shown in Fig. 13.

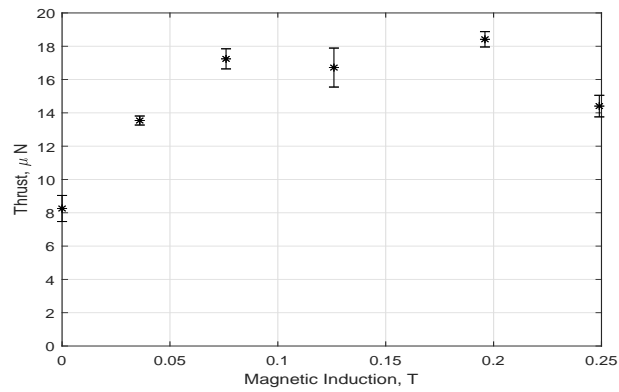


Figure 12: Average thrust versus magnetic induction.

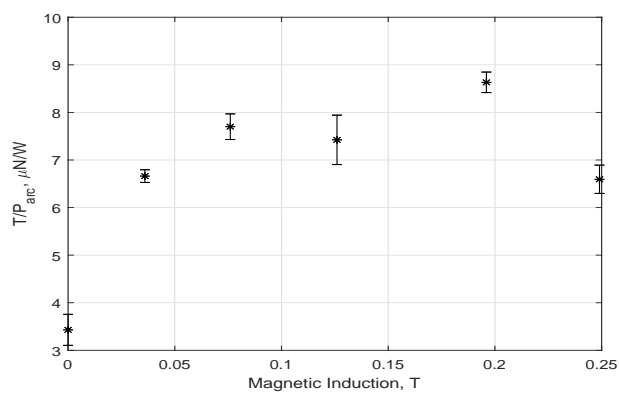


Figure 13: Average thrust to arc power versus magnetic induction.

In the dynamic case we evaluate $\langle \dot{m} \rangle$ from $\langle I_{arc} \rangle$ measurements and Eq. 2. Shown in Fig. 14, \dot{m} increases immediately with the application of magnetic field and only reduces back to non-magnetic values at $B \approx 0.25$ T. Additional rocket performance parameters can be calculated, for example the effective specific impulse, shown in Fig. 15, defined as:

$$I_{sp} = \frac{T}{\dot{m}g_0} \quad (8)$$

where $g_0 = 9.81m/s^2$. The thruster efficiency, shown in Fig. 16, is defined as:

$$\eta_{thruster} = \frac{T^2}{2\dot{m}P_{arc}} \quad (9)$$

Both rocket performance parameters increase monotonically with B .

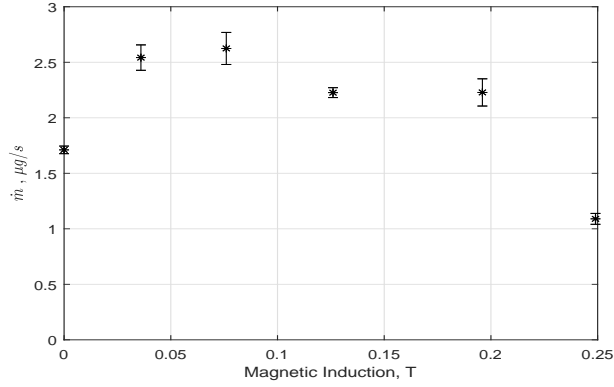


Figure 14: Cathode mass consumption rate versus magnetic induction.

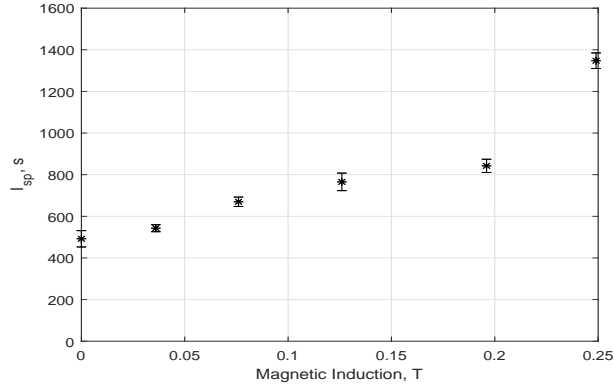


Figure 15: Thruster specific impulse versus magnetic induction.

According to Eq. 5 the axial ion velocity, directed along z , can be evaluated as:

$$u_{i,z} = \frac{T}{\dot{m}_{ion}} = \frac{T}{f_i I_{arc} M_i / (e \langle Z \rangle)} \quad (10)$$

where I_{arc} is the average arc current measured from Q_{arc}/t_{fc} , $M_i \approx 7.95 \times 10^{-26}$ kg is the Ti ion mass, $Z \approx 2.04$ [15], $f_i \approx 0.06$ is evaluated in Ref. [16] for the non-magnetic

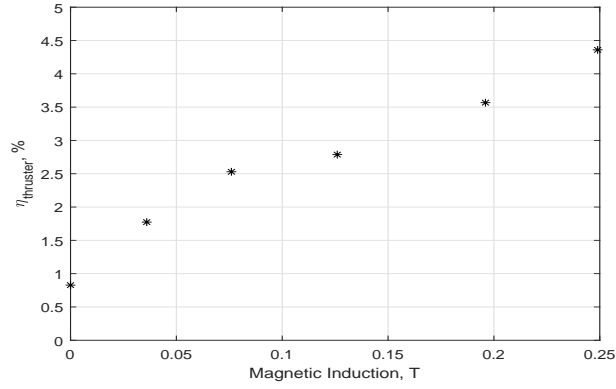


Figure 16: Thruster efficiency versus magnetic induction.

ISF-VAT. Fig. 17 shows the calculated $u_{i,z}$ variation with B where we observe three distinct regions, each contributing ~ 5 km/s to the ion speed. The physical reason for this segmentation is discussed next section.

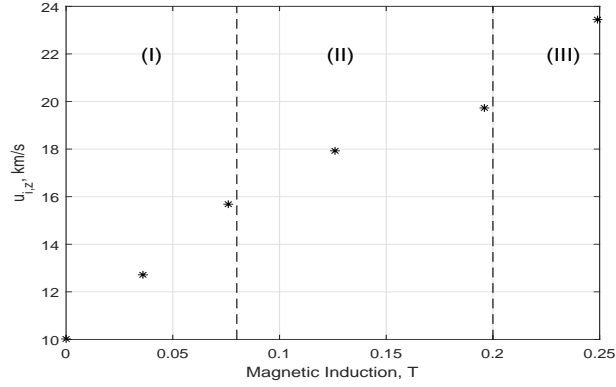


Figure 17: Experimentally evaluated ion velocity versus magnetic induction. The three regions are denoted by vertical lines

4. Discussion

4.1. Performance enhancement by beam collimation

The ion beam of the non-magnetic ISF-VAT was characterized in Ref. [17]. It was shown that the mean ion velocity $\langle u_i(B=0) \rangle \approx 16$ km/s irrespective of the observation angle, and the ion current follows a cosine distribution. In this case we can express the ion current spatial distribution by:

$$dI_i = \frac{I_i}{\pi} \cos\theta \sin\theta d\theta d\phi \quad (11)$$

where, $\sin\theta d\theta d\phi$ is the solid angle differential, θ and ϕ are the azimuthal and polar angles defined with respect to the z direction (i.e., perpendicular to the anode-cathode

plane). Therefore the differential ion current in the z direction can be defined as:

$$dI_{i,z} = dI_i \cos\theta = \frac{I_i}{\pi} \cos^2\theta \sin\theta d\theta d\phi. \quad (12)$$

By integrating Eq. 12 over a hemisphere we obtain the well known beam divergence factor for cosine distribution [16]:

$$C_t^{\cosine} = \frac{I_{i,z}}{I_i} = \frac{1}{\pi} \int_{\phi=0}^{2\pi} \int_{\theta=0}^{\frac{\pi}{2}} \cos^2\theta \sin\theta d\theta d\phi \approx 0.67 \quad (13)$$

According to this result we expect that for a fully collimated beam the axial ion velocity will be $u_{i,z} \approx 16$ km/s. This is indeed obtained for $B = 0.07$ T which is 50% greater than the non-magnetic case. Therefore the increase in ion speed in region I of Fig. 17 can be explained by beam collimation alone.

4.2. Performance enhancement by magnetic nozzle effect

As shown in region II of Fig. 17 the ions are further accelerated in the plume. Such acceleration can be explained by the magnetic nozzle effect. In a magnetic nozzle electron thermal energy is converted to directed (axial) ion energy via ambipolar electric field. Here we follow a 1D magnetic nozzle model detailed in Ref. [18]:

$$\hat{R}_v^2(\hat{z}) \hat{n} M = M_0; \hat{n} = e^{\hat{\phi}}; M = \sqrt{(M_0^2 - 2\hat{\phi})} \quad (14)$$

where \hat{z} is the normalized distance, \hat{R}_v is the normalized plasma cross-section radius, \hat{n} is the normalized density, M is the Mach number, and $\hat{\phi}$ is normalized electric potential. The Mach number is defined as $M = u_{i,z}/c_s$ where $c_s = \sqrt{ZT_e/M_i}$ is the plasma ion acoustic speed. It is known that in vacuum arcs electron temperature $T_e \approx 3$ eV [19, 16], therefore $c_s \approx 3.5$ km/s. Due to the quasi 1D nature of the model, it is valid only when the plasma enters the nozzle is fully collimated. Such conditions are obtained in our case for $B \gtrsim 0.07$ T and $M_0 \approx 4.5$ (where $u_{i,z} \approx 16$ km/s), i.e. the ions are already supersonic when entering the nozzle.

In a magnetic nozzle magnetic field lines determine the nozzles shape, and a particular plasma configuration is determined by $R_{v,0}$, i.e. the field line at the plasma edge at the nozzle inlet. The plume image in Fig. 6(b) does not allow accurate determination of $R_{v,0}$, instead, we denote two possible outliers: $R_{v,0} = 3.8$ mm (green line) and $R_{v,0} = 1.6$ mm (blue line). The magnetic nozzle topology for $R_{v,0} = 1.6$ mm is shown in Fig. 18.

The corresponding solutions $M(z)$ of Eq. (14) for the two $R_{v,0}$ are shown in Fig. 19. For convenience we added the experimental Mach number for $B = 0.07$ T, $B = 0.126$ T and $B = 0.2$ T. We observe that the longer nozzle can accommodate the ion velocity increase evaluated for region II of Fig. 17.

However, the limitations of Eq. (14) are apparent at $B \approx 0.25$ T, indicated as region III in Fig. 17. The experimentally derived Mach number $M \approx 6.7$ is too high for the model to account, requiring very small $R_{v,0}$ and the nozzle length becomes so large that detachment is probable [20]. Moreover, we can observe in Fig. 6(c) that for this case the plume cross section is $2R_{v,0} \lesssim 1.8$ mm, that is smaller than the anode diameter. This can lead to a strong effect on the arc discharge itself. Indeed, Fig. 5 shows that V_{arc} increased by more than 20 V compared to lower magnetic induction values.

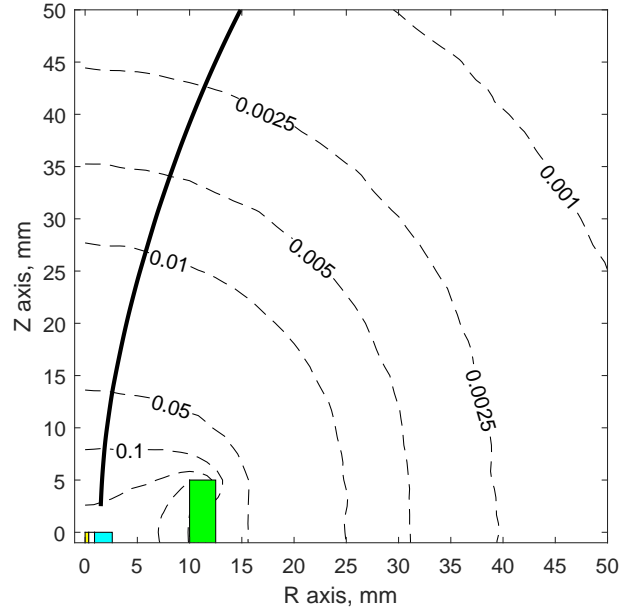


Figure 18: ISF-VAT and air coil magnetic topology showing magnetic field lines for $B = 0.2$ T and the magnetic streamline (nozzle) corresponding to the plasma edge $R_{v,0} = 1.6$ mm (thick black line). Also denoted are the cathode (yellow-box), insulator (white-box), anode (Cyan box), and air coil (green-box) positions.

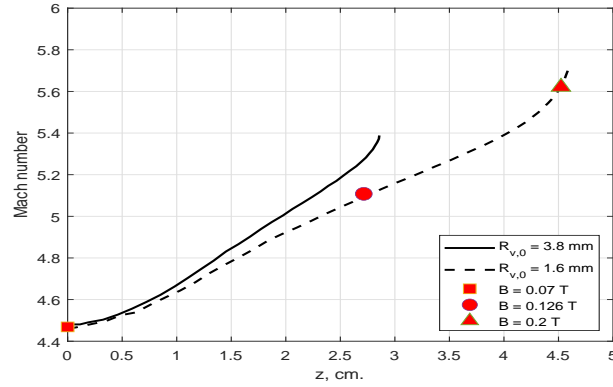


Figure 19: Ion Mach number M versus z for $R_{v,0} = 3.8$ mm (solid line) and $R_{v,0} = 1.6$ mm (dashed line). Markers represent evaluated Mach number from the experiment at $B = 0.07$ T (square), $B = 0.126$ T (circle), and $B = 0.2$ T (triangle).

5. Conclusions

The performance enhancement over non-magnetic ISF-VAT due to application of external magnetic field is shown to be substantial. Between $0 < B < 0.07$ T the ion beam collimation can explain the increase in thruster performance whereas, at intermediate magnetic induction values $0.07 < B < 0.2$ T a magnetic nozzle effect can explain the further improvement in performance. At the highest magnetic induction

studied $B \approx 0.25$ T the arc discharge is significantly affected, the arc voltage increases and the plume diameter contracts considerably.

Acknowledgments

We thank Matteo Laterza for his help with the experimental setup. This work was funded by the Israeli Ministry of Science, Technology and Space.

References

- [1] Levchenko I, Bazaka K, Ding Y, Raitses Y, Mazouffre S, Henning T, Klar P J, Shinohara S, Schein J, Garrigues L *et al.* 2018 *Appl. Phys. Rev.* **5** 011104
- [2] Kronhaus I, Schilling K, Pietzka M and Schein J 2014 *J Spacecr Rockets* **51** 2008–2015
- [3] Jüttner B 2001 *J. Phys. D: Appl. Phys.* **34** R103
- [4] Beilis I I 2001 *IEEE Trans. Plasma Sci.* **29** 657–670
- [5] Kolbeck J, Anders A, Beilis I I and Keidar M 2019 *J. Appl. Phys.* **125** 220902
- [6] Keidar M, Schein J, Wilson K, Gerhan A, Au M, Tang B, Idzkowski L, Krishnan M and Beilis I I 2005 *Plasma Sources Sci. Technol.* **14** 661
- [7] Keidar M, Zhuang T, Shashurin A, Teel G, Chiu D, Lukas J, Haque S and Brieda L 2014 *Plasma Phys. Control. Fusion* **57** 014005
- [8] Kronhaus I, Laterza M and Maor Y 2017 *Rev. Sci. Instrum.* **88** 043505
- [9] Kronhaus I, Chowdhury S and Laterza M 2019 Axial magnetic field effect on vacuum arc thruster performance *36th International Electric Propulsion Conference, IEPC-2019-662, Vienna, Austria*
- [10] Kronhaus I 2019 Inline screw feeding vacuum arc thruster u.s. Patent App. 16/310,175
- [11] Tang B, Idzkowski L, Au M, Parks D, Krishnan M and Ziemer J 2005 Thrust improvement of the magnetically enhanced vacuum arc thruster (mvat) *International Electric Propulsion Conference, IEPC* vol 304 p 2005
- [12] Zhuang T, Shashurin A, Denz T, Keidar M, Vail P and Pancotti A 2014 *J. Propul. Power* **30** 29–34
- [13] Seifert B, Reissner A, Buldrini N, Plesescu F, Scharlemann C, Bulit A and del Amo J G 2013 Development and verification of a μ n thrust balance for high voltage electric propulsion systems *33rd International Electric Propulsion Conference, Washington, DC*
- [14] Laterza M and Kronhaus I 2019 Analysis of erosion and redeposition processes in coaxial vacuum arc thrusters *36th International Electric Propulsion Conference, IEPC-2019-661, Vienna, Austria*
- [15] Polk J E, Sekerak M J, Ziemer J K, Schein J, Qi N and Anders A 2008 *IEEE Trans. Plasma Sci.* **36** 2167–2179
- [16] Anders A 2009 *Cathodic arcs: from fractal spots to energetic condensation* vol 50 (Springer Science & Business Media)
- [17] Kronhaus I, Laterza M and Linossier A R 2018 *IEEE Trans. Plasma Sci.* **46** 283–288
- [18] Ahedo E and Merino M 2010 *Phys. Plasmas* **17** 073501
- [19] Grondona D, Kelly H and Minotti F 2006 *J. Appl. Phys.* **99** 043304
- [20] Ahedo E and Merino M 2009 Acceleration of a focused plasma jet in a divergent magnetic nozzle *31st International Electric Propulsion Conference, IEPC-2009-002, Michigan, USA*